SI Appendix for

Cooperation and spatial self-organization determine rate and efficiency of particulate organic matter degradation in marine bacteria

Authors: Ali Ebrahimi[*], Julia Schwartzman[*], Otto X. Cordero[†]

[†]Corresponding author: Otto X. Cordero, Email: ottox@mit.edu
*these authors contributed equally to this work.

This PDF file includes:

SI methods
Figs. S1 to S10
Tables S1 to S3
References for SI reference citations

SI Methods

Individual-based modeling procedure

Growth and division

The individual-based model assumes that an individual cell doubles to two identical cells after a certain amount of carbon is taken up (1, 2). In this model, a Monod-kinetic parameterization (3) gives the carbon uptake kinetics of individual cells v_i^s and their biomass accumulation:

$$v_i^s = V_{\max} B_i \frac{[C]}{[C] + K_s} \quad (1)$$

where B_i is the cell dry mass of the individual cell, *i,* and the maximum rate of substrate uptake is: $V_{\max} = \mu_{\max} / Y_{\max}$ (maximum specific growth rate / growth yield). K_s is the half-saturation constant for dissolved oligosaccharide. We assume that dissolved oligosaccharides [*C*] are the primary limiting substrate for growth, and that all other nutrients (e.g., sources of phosphate and nitrogen) are available at non-rate limiting levels.

For cell *i*, the actual biomass accumulation ($\frac{dB_i}{dt} = v_i^s Y_{\max}$) and resources consumed ($\frac{dB_i}{dt} = B_i m_i Y_{\max}$) for maintenance, m_i are both assumed to be proportional to the cell's dry mass, B_i, therefore, the net growth in the cell biomass (μ_{net}) can be described as follows:

$$\mu_{net} = \left(\frac{v_i^s}{B_i} - m_i \right) Y_{\max} \quad (2)$$

The minimum volume of the individual cell at division ($V_{d,min}$) is estimated from the descriptive Donachie model (1, 2)

$$V_{d,min} = 2\overline{V_u} / 1.433 \quad (3)$$

where $\overline{V_u}$ is median volume of the individual cell. If the individual cell volume becomes larger than $V_{d,min}$, the parent cell divides to form two new daughter cells. The individual cells are assumed to be cylindrical. It should be noted that the actual growth kinetics of an individual cell could be limited due to substrate availability within the corresponding mathematical mesh grid (M_s) at each time step (Δt), therefore if the uptake driven by Eq. 1 is higher than the available substrate in a given mesh grid ($M_s < \sum_n \Delta t.\nu_i^s$) then the available substrate is equally shared among the number of individuals inhabiting the same grid ($\nu_s^{tot.} = M_s / n$, *n*: number of individuals within the same mesh grid). The biological parameters of the kinetic microbial model are summarized in Table S2.

Microbial active movement

Microbial movement is modeled as flagellar motility: a self-propulsive force guided by chemotaxis that is driven by local substrate gradients (4, 5). The model describes the chemotactic movement of an individual bacterium as a biased-random walk where the flagella propel a straight “run” by rotational movement of the motor and then reverse the rotation to switch direction with a probability to change direction (“tumble”) set by surrounding gradients of chemo-attractants. To apply chemotactic movement to single cells at each time step, the sensitivity of microbial chemoreceptors towards higher substrate concentrations are described using a receptor model that uses the specific growth rate as the chemotactic potential (6, 7). Thus, in the biased random walk of an individual bacterium, the probability of transition $P_{move,i}$ in a tumbling event into a new (more favorable) direction from the current direction (previous “run”) is expressed quantitatively as(1, 6):

$$p_i(t) = \frac{\exp(\alpha_i \nabla \mu_j(t))}{\sum_{j=1}^{m} \exp(\alpha_i \mu_j(t))}, \quad (4)$$

$$\alpha = \frac{X_0}{2\mu_{\max} v_{1D}} \quad (5)$$

Where α is the factor for the chemotactic motion derived from chemotactic sensitivity coefficient of individual cells to chemo-attractant(8), X_0, bacterial maximum swimming velocity, v_{1D} and the growth rate in response to local gradients, μ_{max} . m is the number of directions that an individual cell could sense the local gradients in 3D surrounding environment. To insure homogenous directional choices, the summation is evaluated with a relatively high number of possible directions (m=20) for each individual cells. This number was chosen because it presents many possible directions, and minimizes the computational burden when scaling up to systems of thousands of individual cells. The distance in which bacterial cells sense a local chemotactic gradient is set equal to the cell length (1 μm). Periodic boundary conditions are assumed for bacterial cells that pass outside of the external boundaries of the system.

Bacteria-particle interactions

Bacterial cells are allowed to attach to the particle surface when they stochastically encounter a particle. The model assumes that bacterial cells attach to the particle upon surface encounter, but that a set detachment probability for each cell allows them to detach from the particle. This probability is invariant over the span of time that cells are surface-associated, which contrasts with many characterized mechanisms by which bacteria form irreversible contact with surfaces(9). To determine the effect of this simplifying assumption on the behavior of the model, we simulated a wide range of detachment probabilities, ranging from no detachment to a relatively high detachment rate (1% detachment probability per second).

Enzymatic activity

Cells in the model can broadcast extracellular enzymes. These enzymes are produced at a constant rate that is proportional to the biomass of the cell, and the enzymes can diffuse into the bulk environment. Enzymes that come into contact with the particle subsequently hydrolyze polysaccharide and release diffusible oligosaccharide at the particle surface. The production of enzyme is assumed to be activated when a bacterial cell adheres to the particle, or when cells take up enough oligosaccharide to support cell maintenance. That is, the process of enzyme production preserves mass conservation. We modeled the rate that an individual cell *I* broadcasts enzymes ($S_{E,i}$) as a conditional linear function to its biomass, B_i:

$$\begin{cases} S_{E,i} = K_{enz.} B_i & \left(\nu_i^{act} - B_i m_i\right) > 0 \\ S_{E,i} = 0 & \left(\nu_i^{act} - B_i m_i\right) \leq 0 \end{cases} \quad (6)$$

where ν_i^{act} is the actual uptake rate by the individual cell and *m* is the maintenance rate. The diffusion of the enzyme is then solved by considering a source term, equivalent to the total production rate of enzymes from a corresponding cubic mesh grid ($S_{E,P} = \sum_{i=1:n} S_{E,i}$) and a sink term on the particle source that gives the rate at which enzymes adhere ($S_{A,P}$).

Oligosaccharide diffusion-reaction in physical domain

The model explicitly simulates the loss of oligosaccharides to the bulk environment due to the presence of diffusion or flow. This is implemented by absorbing conditions at the boundaries of the simulated domain in which oligosaccharides that arrive at a boundary are lost to the bulk environment with no accumulation. This is a relevant assumption for many aquatic and terrestrial ecosystems, in contrast to soil ecosystems under dry conditions that may impose restrictions on substrate diffusivity or to batch culture where substrates accumulate in culture vessels.

The transport and uptake of depolymerized oligosaccharides are modelled based on Fick's law of diffusion and mass conservation. We modeled a 3D cubic volume around a single particle and assumed that diffusion of oligosaccharides is the main mode of mass transport. The reaction-diffusion equation is then numerically solved by the finite-difference method, assuming a regular cubic mesh discretization(10):

$$\frac{\partial C_s}{\partial t} = D_s \nabla^2 C_s - S_s + S_{dp} \tag{7}$$

where C_s is the concentration of oligosaccharide (the product of enzymatic hydrolysis), D_s is the diffusion coefficient of the oligosaccharide and S_s is the oligosaccharide consumption rate (the sink term) due to microbial uptake. S_s is a summation of the individual uptake rates (v^s), of all cells within a cubic mesh grid ($S_s = \sum_{i=1:n} v_i^s$, n is the number of individuals in the mesh grid) (10). S_{dp} is the production rate of oligosaccharide given from Eq. 11. The mesh grid size is chosen to be approximately 10 μm and the time step used for simulating oligosaccharide diffusion is the same as that used for chemotactic movement for computational simplicity. For each time step, the Dirichlet boundary conditions are applied for the particle surface and the external boundaries of the cubic volume around the particle. The concentration of oligosaccharide at the external boundaries is set to zero to create an absorbing boundary condition (eliminate the accumulation of oligosaccharide). This external boundary condition is similar to that used for enzyme diffusion (below). A convective term is added in the case where oligosaccharide transport processes are modeled around sinking particles.

Enzyme diffusion and decay:

The diffusion of the enzyme is solved by considering a source and sink term, similar to Eq. 7:

$$\frac{\partial C_E}{\partial t} = D_E \nabla^2 C_E + S_{E,P} + S_{A,P} \tag{8}$$

here C_E is the concentration of broadcast enzyme and D_E is the enzyme diffusion coefficient. Both values can be measured experimentally. In this study, we used an empirical model that decomposes the diffusion coefficient into components describing the viscosity η and temperature T of the medium, and molecular weight of the molecule, Mw $D_E = 1.7\times10^{-7} T / Mw^{0.41}\eta$ $(\mathrm{cm}^2/\mathrm{s})$ (11). In Eq. 7, the adhesion of enzyme to the particle acts as a sink term at the particle surface boundary that is equivalent to the total amount of enzyme that arrives at the particle surface ($S_{A,P} = \int_r^{r+\Delta L} C_E dA$, ΔL). The total enzyme accumulation on the particle ($S_{E,surf.}$) is then the integral of the accumulation rate $S_{A,P}$ minus the decay rate, $S_{E,D}$:

$$S_{E,surf.} = \int_0^t S_{A,P} dt - S_{E,D} \tag{9}$$

Enzymes are assumed to decay with first order kinetics, so $S_{E,D}$ is a function of the amount of enzyme adsorbed to the particle surface (12–14):

$$S_{E,D} = K_l S_{E,surf.} \tag{10}$$

where K_l is defined as the enzyme decay coefficient. The depolymerization rate of polysaccharide (S_{dp}) to oligosaccharide is therefore a function of the particle-adsorbed enzyme ($S_{E,surf.}$) with a linear empirical relationship:

$$S_{dp} = K_p S_{E,surf.} \tag{11}$$

where K_p is the particle lability, defined as a lumped parameter that resembles biopolymer and enzyme biochemistries. That is, K_p is a combined term to express difficulty of the particle to degrade relative to the activity of the enzyme produced by the cells.

Oligosaccharide transport in presence of particle sinking

Where we model sinking in our simulations, we assume a constant 1D speed rate along the water column, *u* (see Figure S2). For simplicity, we assume that particle sinking creates a laminar flow around the particle with the same speed as the particle sinking rate. To address the effect of flow on dissolved carbon and enzyme transport, we added advection term to diffusion model for dissolved carbon and enzyme transports (Eq. 7 and 8) and expressed as:

For dissolved carbon:

$$\frac{\partial C_s}{\partial t} + u.\nabla C_s = D_s \nabla^2 C_s - S_s + S_{dp} \quad (12)$$

For enzyme:

$$\frac{\partial C_E}{\partial t} + u.\nabla C_E = D_E \nabla^2 C_E + S_{E,P} + S_{A,P} \quad (13)$$

where sink and source terms for dissolved carbon (S_s, S_{dp}) and enzyme (S_s, S_{dp}) are all expressed similar to equations 7 and 8, respectively. Similar to the stationary particle simulations, the mesh grid size was chosen to be approximately 10 μm and the time step of calculations was assumed to be similar to the time interval between chemotactic tumbles (5 seconds). At each time step, Dirichlet boundary conditions are applied to the particle surface to the external boundaries of the volume around the particle. At the particle surface a constant flux of oligosaccharide production is considered as given by Eq. 11, as a function of the particle-adsorbed enzyme concentration. As above, the external boundary concentration of oligosaccharide is set to zero. A finite difference method was applied to solve Eq. 12 and 13 simultaneously at each time step within the individual-based model.

To model longer time scales of particle sinking in the water column, we implemented a spatial algorithm to only model the effective zone around the particle in each time scale, instead of modeling the whole water column for each time step. Based on analyzing the concentration

gradient of dissolved carbon around the particle, we chose the effective zone as the region with concentration gradient above a threshold value (5% of maximum chemical gradient).

'Population-level' analytical bottom-up model

We developed a simple quantitative model to predict the fold change in biomass based on the measurable physiological and behavioral features of marine bacterial isolates. The model is parametrized based on the rate of enzyme production and activity (degradation rate) to predict the total of oligosaccharide production, *M* over time, given by first order kinetics:

$$\frac{\partial M}{\partial t} = K_{p,m} B_p + V_{\max} B_p \frac{[C]}{[C] + K_s} - \lambda M \tag{14}$$

where $K_{p,m}$ is the rate of oligosaccharide production per biomass per hour that is derived from enzymes bound to the cell membrane. B_p is the particle-associated fraction of the total biomass. $V_{\max} = \frac{\mu_{\max}}{Y}$ is the maximum uptake rate, defined as the ratio of maximum growth rate of bacteria, $\mu_{\max}$ to the yield of substrate conversion to biomass, *Y* (experimentally measured). λ is the fraction of monomers that are lost to the bulk environment and the value is assumed from what we obtained from individual-based model simulations, and from previous reports in the literature about the inefficiency of oligosaccharide recovery from hydrolysis (15). Note that as the enzyme is tethered to the cells, no diffusion for the enzyme is assumed.

The particle-associated biomass production rate is represented based on the combination of Monod-type growth kinetics and attachment-detachment frequencies:

$$\frac{\partial B_p}{\partial t} = \mu_{\max} B_p \frac{[C]}{[C] + K_s} + \alpha_a B_F - \alpha_d B_p \tag{15}$$

where B_F is the fraction of free living biomass in the system, *[C]* is the oligosaccharide concentration, calculated from the ratio of oligosaccharide mass, *M* to the volume. K_s is the half-

saturation constant, experimentally measured in Figure S10G. α_a and α_d are attachment and detachment rates, respectively, derived from measurements in Figure S10B-C.

The change in free-living biomass, B_F is derived from the frequency of attachment and detachment, assuming that free-living cells do not themselves grow:

$$\frac{\partial B_F}{\partial t} = \alpha_d B_p - \alpha_a B_F \quad (16)$$

Experimental methods:

Culture conditions: Strain *psych6C06* was previously isolated from an enrichment of nearshore coastal seawater (Nahant, MA, USA) for surface-associated chitin degrading microbial communities (16, 17). The strain was maintained as colonies on Marine Broth 2216 (Difco 279110) with 1.5% agar (BD 214010). To establish exponential growth, we modified a culturing protocol previously developed for *Escherichia coli* K12 (18). Briefly, single colonies were picked and transferred to 3 mL liquid Marine Broth 2216 and incubated at 25 ºC, shaking at 150 rpm on a VWR DS-500 orbital shaker to establish seed cultures. Seed cultures were harvested after ~5 hours by centrifugation for 1 min at 5000 rcf (Eppendorf 5415D, Rotor F45-24-11). The supernatant was discarded and serial dilution of the cells were used to establish pre-cultures in pH 8.2 minimal media supplemented with 20 mM *N*-acetylglucosamine (GlcNAc). The core minimal medium contained the major ions present in seawater, plus vitamins and trace minerals per L: 20 g NaCl, 3 g $MgCl_2$-$6H_2O$, 0.15 g $CaCl_2$-$2H_2O$, 0.05 g KCl, 2.1 mg $FeSO_4$-$7H_2O$, 30 µg H_3BO_3, 100 µg $MnCl_2$-$4H_2O$, 190 µg $CoCl_2$-$6H_2O$, 2.2 µg $NiSO_4$-$6H_2O$, 2.7 µg $CuSO_4$, 144 µg $ZnSO_4$-$7H_2O$, 36 µg Na_2MoO_4-$2H_2O$, 25 µg $NaVO_3$, 25 µg $NaWO_4$-$2H_2O$, 2.5 µg SeO_2, 100 µg riboflavin, 30 µg D-biotin, 100 µg thiamine-HCl, 100 µg L-ascorbic acid, 100 µg Ca-$_D$-pantothenate, 100 µg folate, 100 µg nicotinate, 100 µg 4-aminobenzoic acid, 100 µg pyridoxine HCl, 100 µg lipoic acid, 100 µg nicotinamide adenine dinucleotide, 100 µg thiamine pyrophosphate, and 10 µg cyanocobalamin. In addition to the carbonate buffer present in the

core minimal medium (reflecting natural seawater buffering capacity), we added 50 mM HEPES buffer pH 8.2 to control for the effects of heterotrophic metabolism on pH. We also supplemented the core medium with10 mM NH4Cl, 1 mM Na_2PO_4, and 1 mM Na_2SO_4 to create a carbon-limited minimal medium. Where appropriate, we supplemented with the *N*-acetyl-$_D$-glucosamine (GlcNAc, concentrations indicated). Following overnight growth at 25 ºC, the cell density was measured in 1 cm cuvettes by absorbance measurements at 600 nm (A_{600}) using a Genesys 20 spectrophotometer. Under these conditions, A_{600} 1.0 =8x10^8 cells/mL, measured by serial dilution and plating.

Measurement of Monod growth parameters

To measure the maximum growth rate on GlcNAc, cells were prepared as described above, then diluted to a starting A_{600} of 0.01 in 4 mL of fresh 20 mM GlcNAc minimal medium in a 10 mL vented polystyrene tube. Absorbance measurements were taken over time, and the linear regression was fit to the plot of ln(A_{600}) vs. time. The slope of this regression is equivalent to the growth rate. To measure the half-saturation constant, cells were diluted from a A_{600} 1.0 by a factor of 10^5 into carbon-free minimal medium, and 100 µl of this dilution was used to inoculate medium containing a GlcNAc at different concentrations (221, 110, 22, 11, 2.2, 1.1, 0.22, 0.11, and 0.02 mg/L). At 2 h time intervals, 100 µl of this culture was plated onto MB 1.5% agar plates. The resultant colonies were counted, and the change in colony numbers over time was used to derive the growth rate. The maximum growth rate measured by this method was the same as that measured using the A_{600}-based approach. Growth rate was plotted against carbon concentration (S), and the experimentally measured µ and S were fit to the Monod growth equation ($\mu=\mu max(S/(S+K_{sat}))$ to derive parameters µmax and K_{sat} using a least squares fit with a maximum of 1000 iterations. The biomass yield during growth on GlcNAc was derived from direct measurement of cell density (A_{600}) and GlcNAc depletion using the dintrosalicylic acid reagent method to colorimetrically quantify reducing sugars in cell-free media (19). The grams

of GlcNAc/mL depleted from the media was plotted against the grams of cells produced, at timepoints covering three population doublings (A_{600} 0.1-0.8). The mass of an individual cell was assumed to be 19 fg: a value which we derived from scaling the measured mass of individual *E. coli* with 60 min doubling time (220 fg, (20)), by the growth rate of *psych6C06* (0.35), and also by a factor of 4 to reflect a linear increase in biomass per cell with osmolarity between M9 and seawater (21), divided by the ratio of *E. coli* to *psych6C06* volume (16:1).

Measurement of protein production and enzymatic activity

To collect secreted protein and cell-associated protein, cells were grown in large batches. Cells were prepared for inoculation as described above, and inoculated at an initial density of A_{600} 0.01 into 250 mL Erlenmeyer flasks containing 150 mL of 20 mM GlcNAc minimal medium. The flasks were grown with 150 rpm shaking at 25 ºC. Periodically, 25 mL of culture was removed from the flasks, and centrifuged at 5000 rcf for 10 min at 4 ºC. Sampling was stopped when the culture flask volume reached 75 mL, past which point culture growth rate was affected by volume. The supernatant was collected and filtered through 0.2 µm Sterivex filters (EMD Millipore), at which point protease inhibitor (Roche cOMplete) was added. The pellet was immediately frozen at -20 until quantification. Supernatant was concentrated ~50 x in Amicon Ultra 3 kDa centricon tubes (EMD Millipore), and rinsed twice with 12 mL of carbon-free minimal media to remove small molecules and other potentially inhibitory compounds. The protein abundance was quantified by measuring absorbance at 280 nm, with a 340 nm pathlength correction on a Nanodrop spectrophotometer (Thermo Scientific). The quantification was calibrated using standards of from proteins of known concentration (BSA, chitinase). Chitinase activity was quantified using Methylumbelliferyl-conjugated substrates N,N′-diacetyl-β-D-chitobioside, N-acetyl-β-D-glucosaminide, and β-D-N,N′,N″-triacetylchitotriose (Sigma CS1030). Briefly, 2.5 µl of a 20 µg/mL stock of each substrate in DMSO was added to 197.25 µl of concentrated protein or crude cell lysate in chitinase assay buffer (carbon-free minimal medium,

pH 8.2 with no vitamins, ammonium or phosphate). The amount of cell lysate was normalized prior to assay. The accumulation of fluorescence (ex 360-20/em 450-20) was monitored on a Tecan Spark at 25 °C with a cooling module, by measuring fluorescence signal accumulation at 2-minute intervals with continuous shaking at 54 rpm with 6 mm amplitude. Serial dilutions of an unconjugated 4-Methylumbelliferone standard were used to establish the linear range of the instrument and to convert fluorescence intensity into mg/mL of released oligosaccharide.

Bacterial colonization on particles

Precultures with A_{600} between 0.1-0.3 were prepared as described above and used to colonize magnetic chitin hydrogel particles. To prepare the particles, 500 µl of particle slurry was washed 3 times with carbon-free minimal media using magnetic pulldown. The washed particles were further diluted 1:3 and used to fill 15 mL conical tubes. The particle density in the tubes was counted, and all replicates contained between 200-250 particles per mL with size range from 40 to 100 µm in diameter. This density of particles is consistent with previous studies of community assembly (17), and provides the equivalent of about 100 µM of the monomeric unit of chitin, *N*-acetylglucosamine (GlcNAc) to the system. The particles were rotated end over end, so that they fell through the medium due to gravity and remained constantly suspended. Because of the rotation, we were unable to continuously observe the particles and instead sub-sampled the population and made individual measurements of multiple particles at each sampled timepoint. The density of inoculated cells was set to be at an A_{600} of 0.01, diluted from 20 mM GlcNAc minimal medium cultures prepared as described above. A vertical wheel (Stuart S3B, 10” diameter wheel) was used to rotate the 15 mL tubes at 5 rpm at room temperature (21-25 °C) with overhead rotation. To visualize particles and their surface-associated bacteria, 200 µl subsamples were stained with the DNA-intercalating dye SYTO9 (Thermo Fisher, S34854) at a 1:285 dilution of the stock in 96-well plates with optically clear plastic bottoms (VWR 10062-900).

To avoid evaporation from the wells, sterile self-adhesive sealing films were used to seal the 96-well plates.

Confocal microscopy and image processing:

Microscopy was performed on micro-confocal high-content imaging system (ImageXpress Micro Confocal, Molecular Devices), using the 60 µm pinhole spinning disk mode. Fluorescent signal was visualized with a LED light cube (Lumencore Spectra X light engine), and bandpass filters (ex 482/35 nm em 538/40 nm dichroic 506 nm), with a 40x objective (Nikon Ph 2 S Plan Fluor ELWD ADM 0.60 NA cc 0-2 mm, correction collar set to 1.1), and a sCMOS detector (Andor Zyla, pixel size 6.5 µm). To visualize individual particles, particles were manually centered in the field of view and then 100 µm image stacks sampled at Nyquist were acquired in the Z plane using MetaXpress software (version revision 31201). Image analysis was performed in MATLAB (release 2018a). Briefly, image stacks were split in half and a maximum intensity projection was obtained for each half. The low level of fluorescent signal associated with free dye in the hydrogel particles was used to define an intensity threshold suitable to create a binary mask for the particle projections. A mask of the cells within the particles was then defined using their brighter fluorescence intensity. We used this segmentation to quantify the total surface area occupied by the cells on the particle, and to quantify the total surface area occupied by patches. We define patches as an area greater than that equivalent to three cells (>10 μm^2), where cells contact other cells, or were in close proximity (<10µm from nearest neighbor). This definition is analogous to the spacing constraints defined in the individual-based simulation.

To measure cell attachment rates, we converted measurements of cell density on the particle surface into the total number of cells per particle. We assumed that, in the first 4 h of colonization, the accumulation of cells on the particle was due only to attachment. For data points within this time window, we calculated the total number of cells on each particle surface: we multiplied the measured fractional area occupied by cells on a particle by the measured

mean area of an individual cell (0.5 μm^2) and the measured mean surface area of each particle (four times the cross-sectional area assuming that particles are spherical). To obtain the fraction of the initial population of cells that accumulated on a particle surface, we divided the number of cells per particle by the initial concentration of cells added to the medium normalized by the initial density of particles. We plotted the fraction of the initial population accumulated on the beads against time, and fit a linear regression model to the data to obtain the rate at which cells encountered the particle. This was repeated for three different initial population sizes to validate the assumption that the initial attachment rate of cells onto particles was constant (Figure S10B).

To measure cell detachment rates, magnetic particles colonized by bacteria were prepared as described above, collected by a neodymium magnet, and resuspended in cell-free and carbon-free minimal medium. Measurement of the cell density on particles before and after the transfer indicated that the pull down did not affect the density of cells on the particle. Measurement of the bead density before and after pull down indicated that there was no appreciable loss of particles during the media exchange. The resuspended particles were incubated with rotation (as described above), and aliquots of the resuspension were collected at <1 h intervals so that the density of cells on the particles could be determined. To calculate the detachment rate from these data, we assumed a constant rate of detachment, and used Taylor expansion of the growth model $N_t=e^{-Koff*t}$, where N_t is the fraction of cells on the particle at time *t* relative to the population initially on the particle (initial population=1), and K_{off} is the detachment rate. Because cells detaching from the particle accumulated in the bulk medium, we confined our analysis to the first three hours following transfer, in which the first (linear) term of a Taylor expansion of the growth model ($N_t=1-(K_{off}*t)$) can be assumed to make the largest contribution. We thus derived the detachment rate K_{off}, by fitting a linear regression to N_t vs. time. Two different initial colonization densities were tested validate that the detachment rate was constant (Figure S10C).

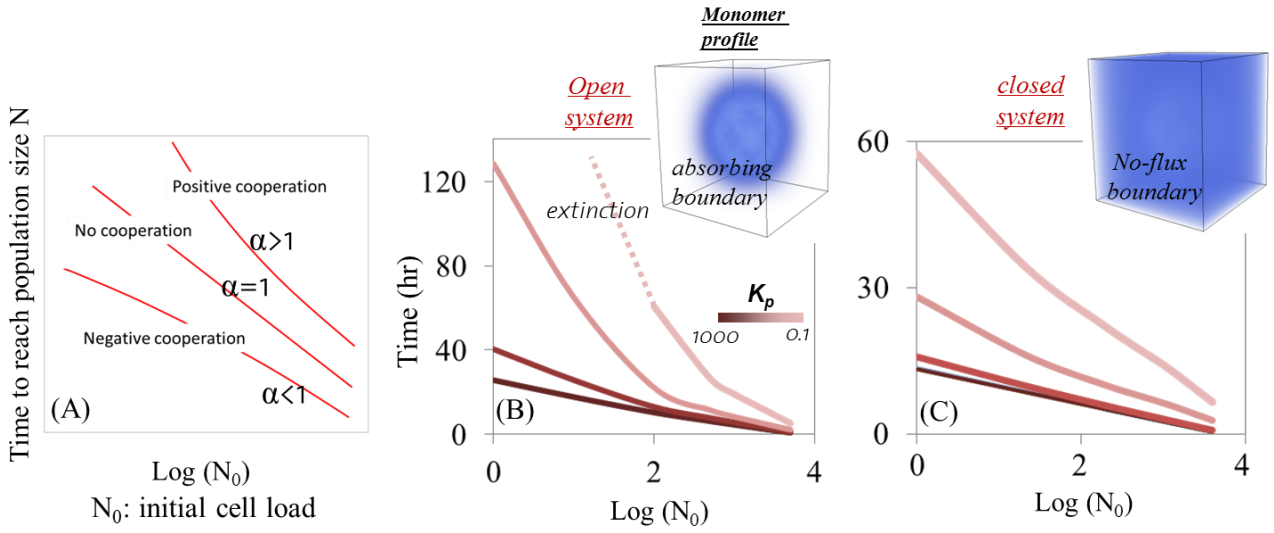

Figure S1. Microbial cooperative behavior affected by batch vs. open systems. Here, a closed system has no flux boundary conditions for bacterial cells, dissolved carbon and enzymes, and an open system has absorbing boundary conditions for dissolved carbon and enzyme and periodic boundary for bacterial cells. A) Cooperative behavior is described as a dependency of bacterial growth rate on the cell initial population size (N_0). It is defined based on a divergence from exponential growth behavior ($Log(\frac{N}{N_0}) = \beta t^{\alpha}$) in which α is 1 for exponential growth and $\alpha > 1$ shows positive cell dependency of growth rate (Cooperative growth). B,C) The dependence of growth rate on initial population size differs for open (B) and closed systems (C). Dashed line indicates the extinction of bacterial community for cell load lower than a threshold value. Inset images indicate the dissolved carbon concentration profiles for their corresponding scenarios. Simulations were done for a particle size of 200 μm and the measurement is defined as the time until the population size reaches 10^5 cells from a starting population of 1000 cells. With limited diffusion, substrates produced from particulate biopolymers accumulate and could eventually be fully consumed (assuming that no other factors limit growth).

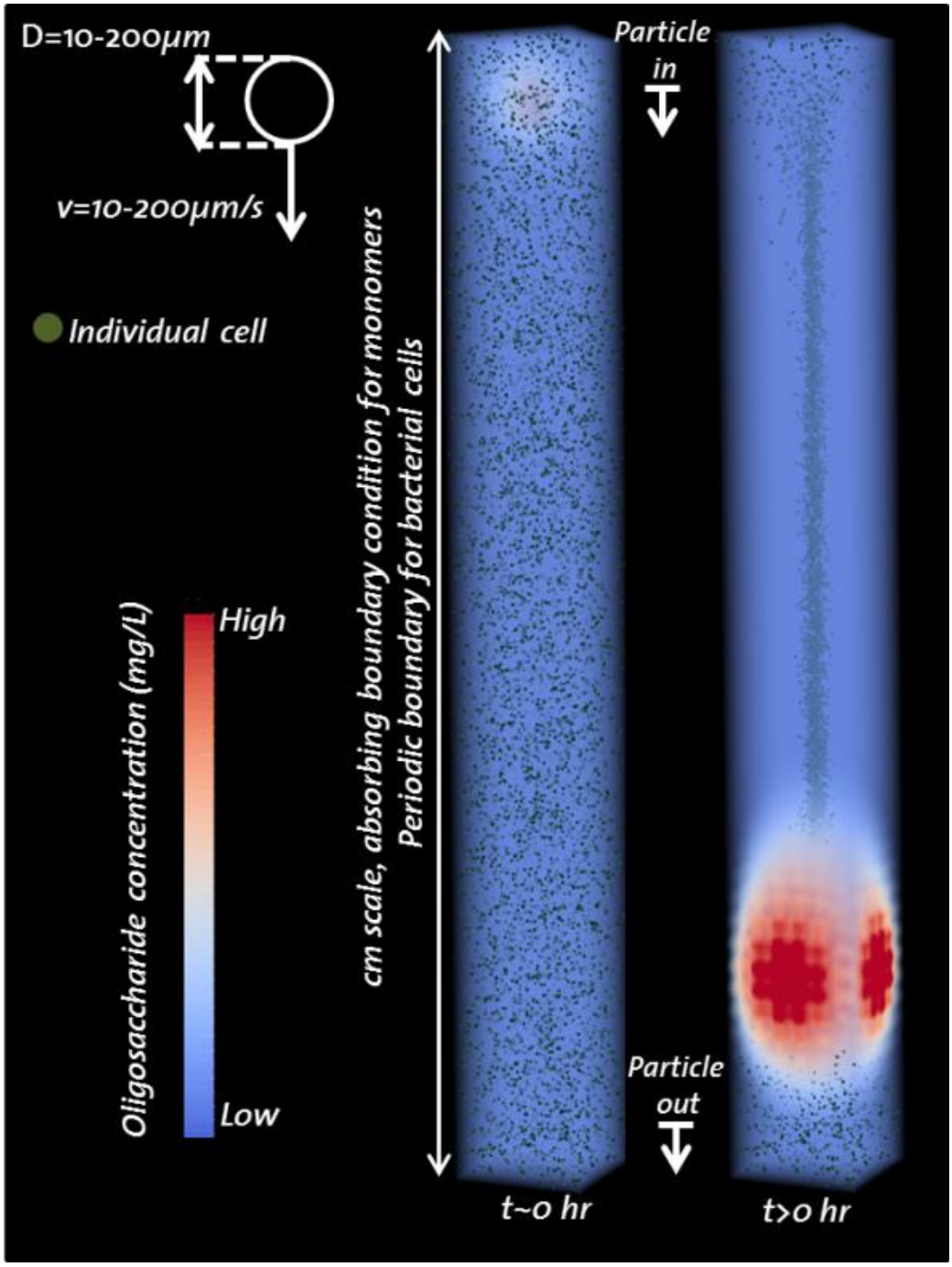

Figure S2. Model description for particle sinking, oligosaccharide profile and individual cell distributions. Individual cells are uniformly distributed over the water column. Each individual is assigned dispersal and enzymatic functions.

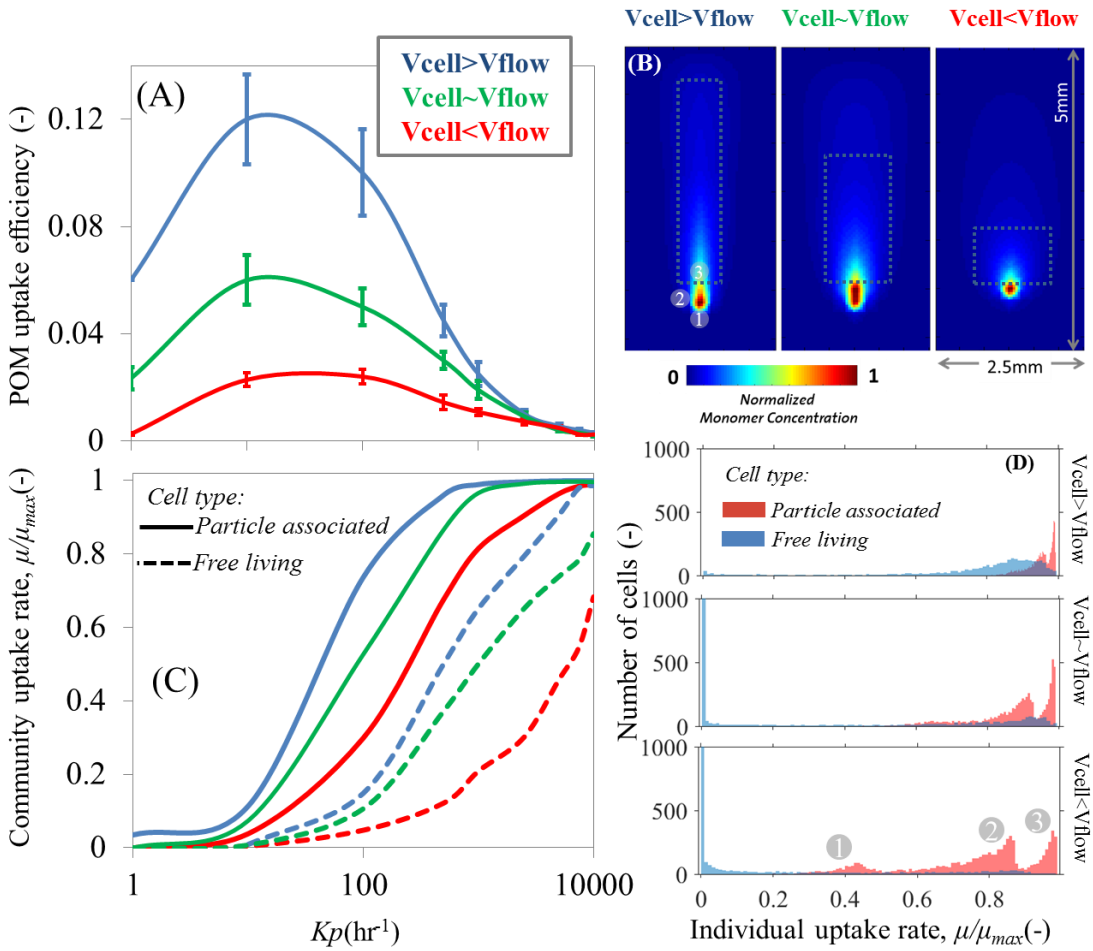

Figure S3. Particle sinking affects local gradients of dissolved organic matter and POM uptake efficiency of particle associated and free-living bacterial cells. A) POM uptake efficiency for a wide range of particle lability affected by the ratio of cell velocity (V_{cell}) to particle sinking speed (V_{flow}). B) Spatial patterns of dissolved carbon concentration around the particle. Concentrations are normalized by the maximum local concentrations for each scenario. C) Mean uptake rate at community level presented for particle associated and free-living bacterial cells. D) Individual cell uptake rate frequencies. The cell velocity is kept constant at 10 µm/s and particle sinking speed is changed from 5 (top) to 10(middle) and 20(bottom) µm/s to evaluate the effects of various ratios. The numbers in grey circle at the peaks of histogram for scenario V_{cell} <V_{flow} corresponds to the individual cells spatial location around the particle in Figure S8B. The results are shown for simulations after 10 hours. Initial cell number is about 10^5 cells/mL uniformly distributed along the depth of the water column. The half-saturation, K_s and maximum growth rate, *µmax* used in this simulation are 0.1 and 0.5, respectively.

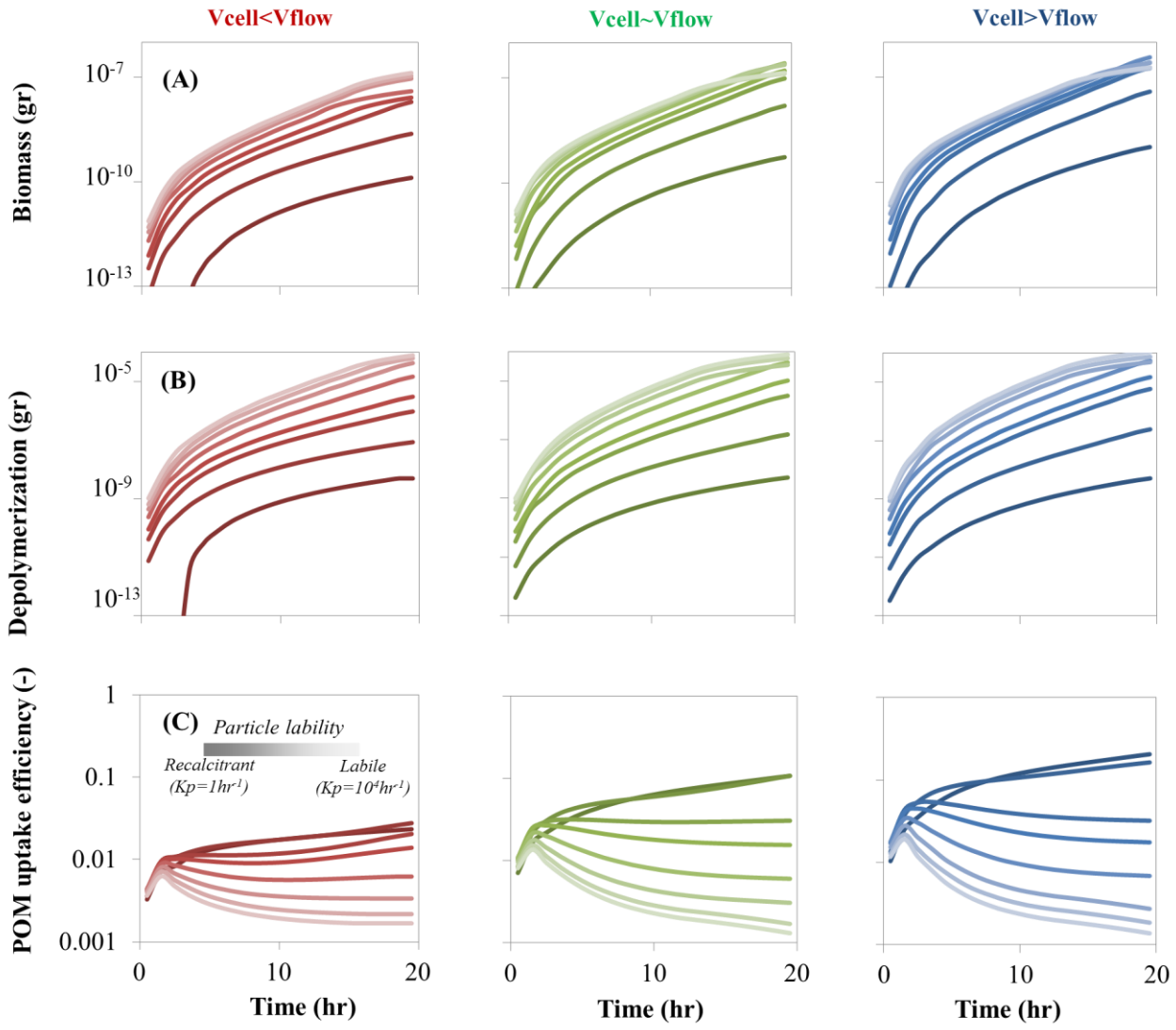

Figure S4. The relative rates of cell motility and fluid flow affect the functioning of polysaccharide degrading populations. Particle sinking affects biomass accumulation A) and depolymerization B) rates and uptake efficiency C). The simulations are performed for 3 ratios of cell to particle sinking speeds. The results are represented for various polymer labilities from labile (Kp=10000 hr^{-1}) to recalcitrant (Kp=1 hr^{-1}). The cell velocity is kept constant at 10 µm/s and particle sinking speed is changed from 5 to 10 and 20 µm/s to evaluate the effects of various ratios. The results are shown for simulations after 10 hours from initializing the simulations. Initial cell number is ~10^5 cells per milliliter volume. The half-saturation, K_s and maximum growth rate, *µmax* are assumed 0.1 and 0.5, respectively. The bacterial cells were initially distributed uniformly in the bulk water.

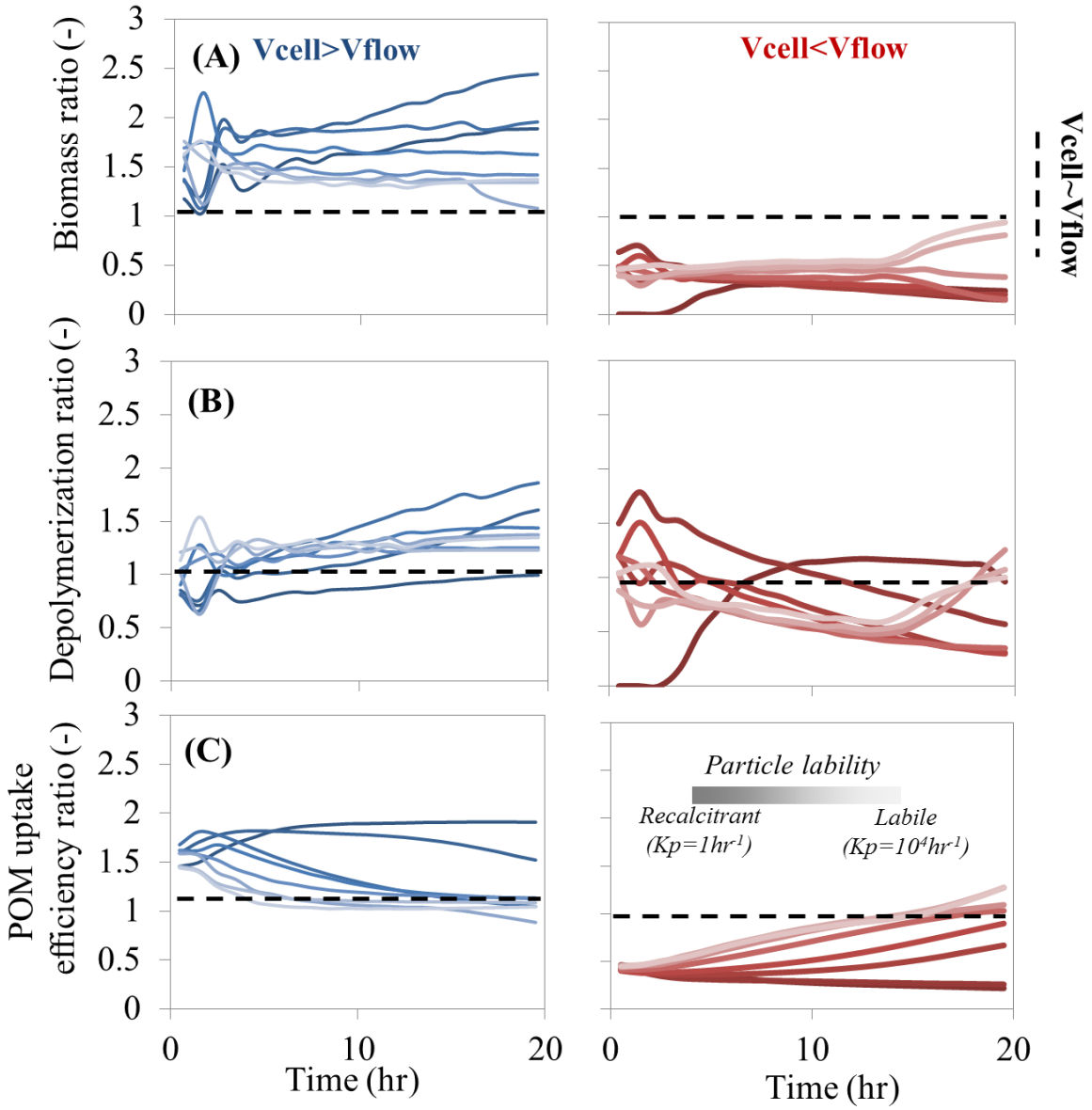

Figure S5. Cells that swim slower than the particle sinking speed are less able to depolymerize polymer, and grow, reflecting inefficient capture of the hydrolysis products. The effect of particle sinking on biomass accumulation A), depolymerization rates B), and uptake efficiency C) is measured against a reference sinking speed. The reference scenario is assumed to be when cell velocity (V_{cell}) and particle sinking speed (V_{flow}) are equal (V_{cell}~V_{flow}). Ratios are calculated by dividing the biomass accumulation, depolymerization and POM uptake efficiency from Figure S9 for two scenarios of particle sinking ($V_{cel} > V_{flow}$ & $V_{cel} < V_{flow}$) with the reference scenario. A ratio of one (dashed horizontal line) indicates that the measured parameter is the same as the reference condition. The half-saturation, K_s and maximum growth rate, μmax are the same as Figure S4. The bacterial cells were initially distributed uniformly in the bulk water.

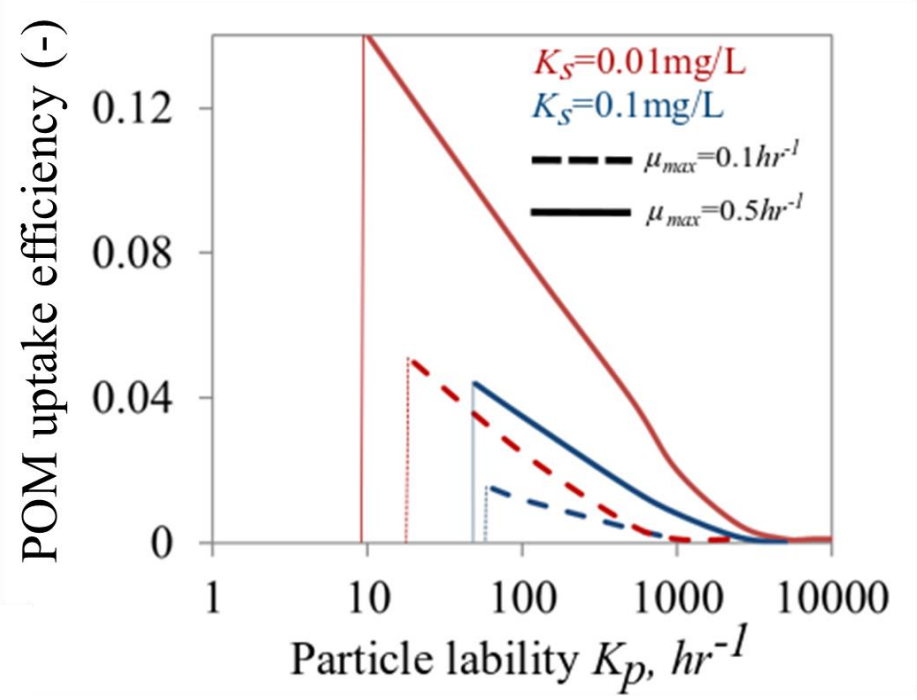

Figure S6. The maximum growth rate μ_{max}, affinity to substrate (K_s) affect POM uptake efficiency in a manner dependent on particle lability (K_p). POM uptake efficiency as a function of particle lability is shown for high (solid lines, μ_{max}=0.5 hr^{-1}) and low (dashed lines, μ_{max} =0.1 hr^{-1}) maximum growth rates. The results are shown for two levels of affinity to substrate (red lines indicate 0.1 mg/L and blue lines indicate 0.01 mg/L). Vertical lines show the threshold particle lability below which no particle degradation and growth/substrate uptake is observed.

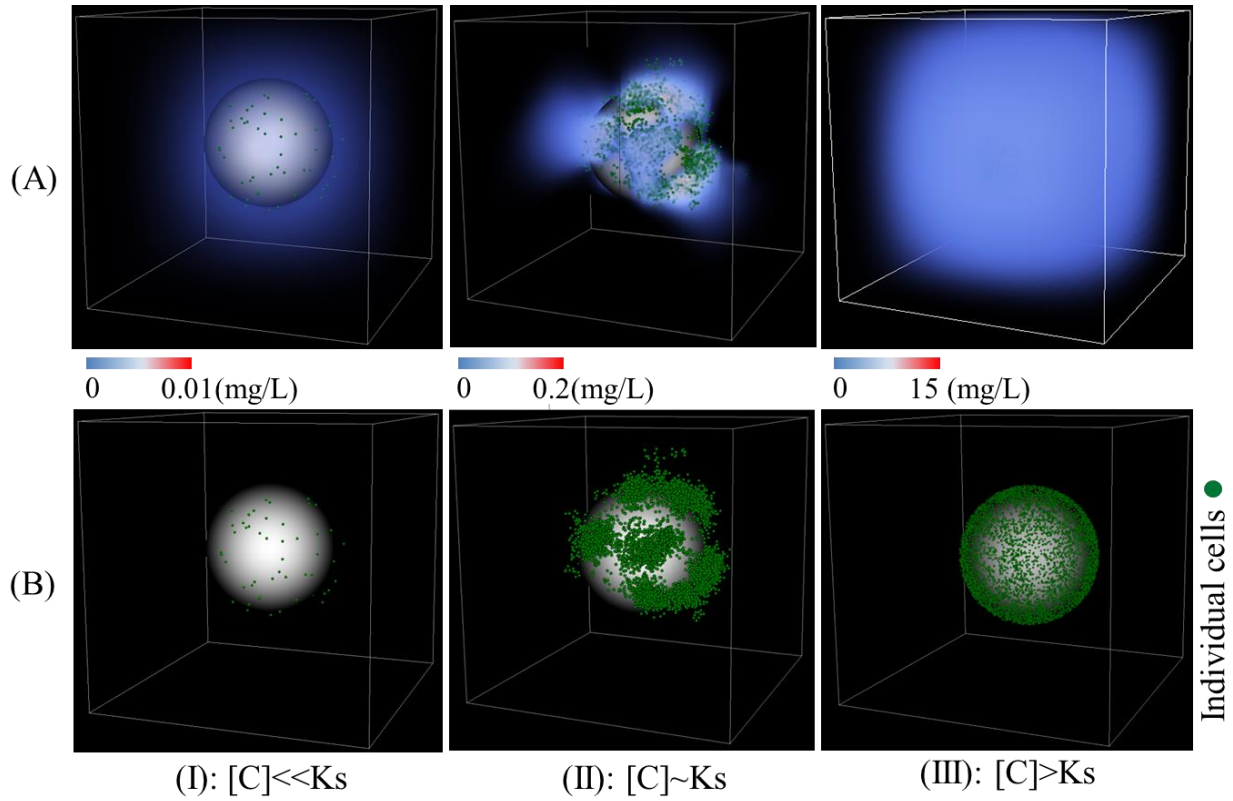

Figure S7. Spatial self-organization and cooperative growth allow degradation of recalcitrant organic particles. A) Dissolved carbon concentration profile. Scale bar shows concentration range, from blue (low), to red (high) projected on microbial population assembly on the particle for three levels of particle lability (recalcitrant I: K_p:1 hr^{-1}, equivalent to [C]<<K_s; semi-labile II: K_p:100 hr^{-1}, equivalent to [C]~ K_s; and labile III: K_p:1000 hr^{-1}, equivalent to [C]>> K_s). [C] indicates the concentration of oligosaccharide available to cells. Green dots show individual cells and B) only shows the bacterial cell colonization on the particle. For visualization purposes, carbon concentrations below a certain threshold are not shown (below 1% of maximum concentration). All simulations were initialized with a particle size of 200 µm and 1000 cells.

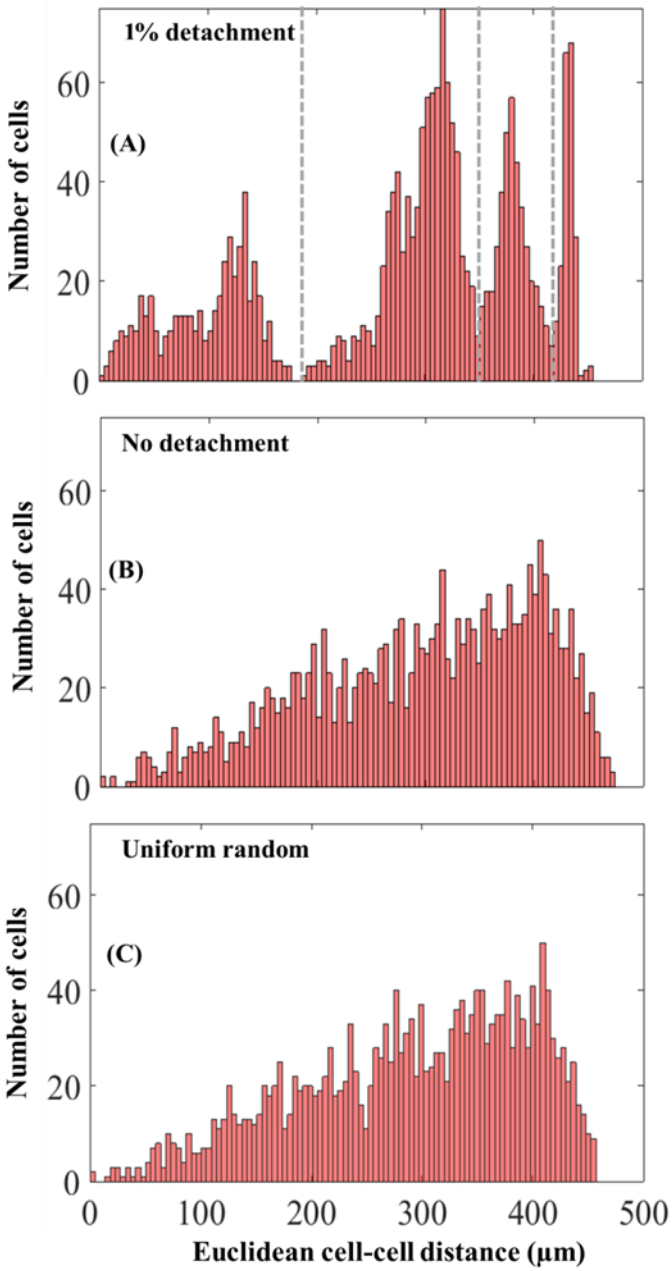

Figure S8. Detachment changes in the distribution of cell-cell distances within particle associated populations. Distribution shown for simulations with 1% detachment (A) or without detachment (B). The simulations were run for semi-recalcitrant particles (K_p=100 hr^{-1}), corresponding to the simulations in Figure 2B with an initial cell density of 1000 and after 10 hours. The dashed grey lines separate single patches. C) A hypothetical scenario with a uniform random distribution of bacterial cells on the particle surface is shown for comparison. In this comparison, the cell-cell distance was calculated between a reference single cell and randomly selected 2000 cells on the particle.

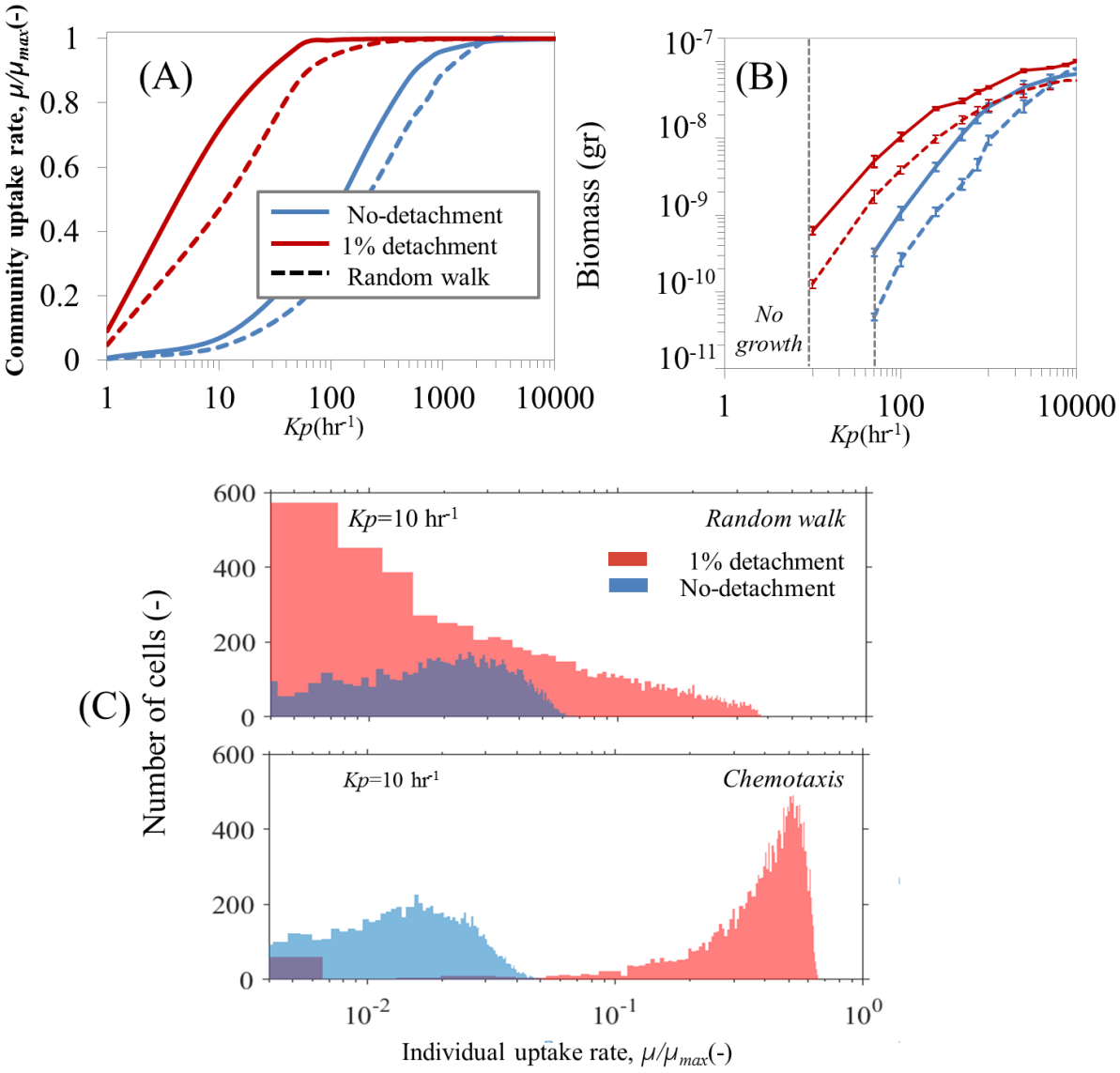

Figure S9. Microbial dispersal strategies regulate POM uptake efficiency from organic particle. A) Effects of individual cell behaviors on mean carbon uptake rates, represented as a function of particle lability (K_p). Chemotactic behavior (solid lines) vs. random walk (dashed lines), are compared with no detachment (blue lines), or 1% detachment (red lines). The mean uptake rate is normalized by the maximum uptake rate of individual cells. B) The effect of individual cell behaviors from panel A, on biomass accumulation after 10 hours. Grey dashed line indicates extinction zone of bacterial population (no biomass accumulation). C) Histogram of individual cell uptake rates for surface-associated cells. The uptake rates after 10 hours of simulation are shown for K_p=10 hr^{-1}, initialized with 10000 cells on 200 µm particles.

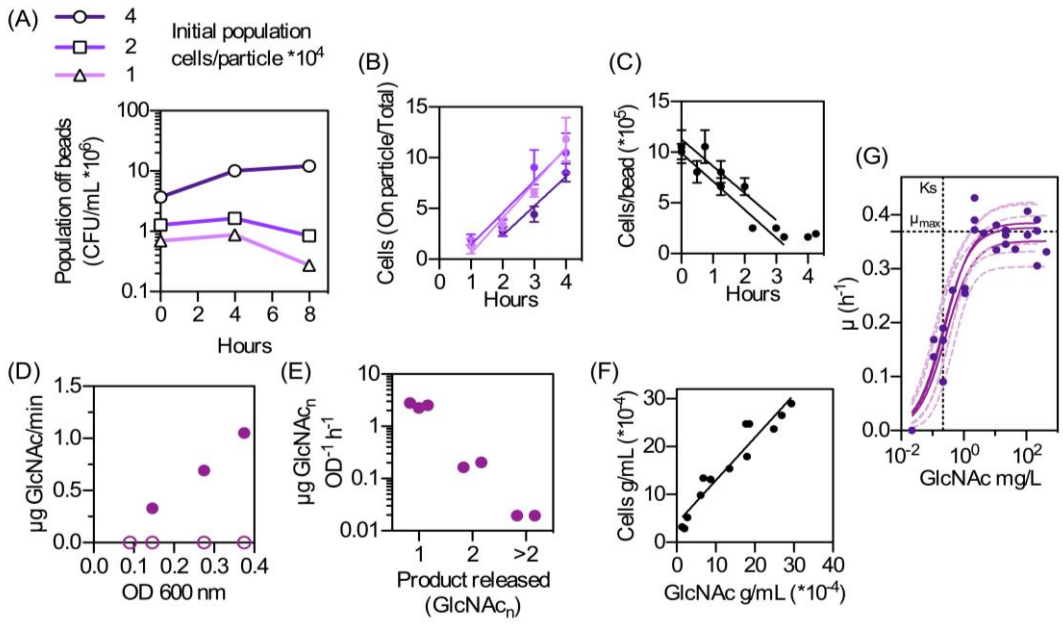

Figure S10. Measurements of *psych*6C06 physiology and behavior used to parameterize the population-level model. A) Viability of *psych*6C06 during colonization of chitin particles. Cells at an initial density of $4*10^4$ per particle are able to colonize and break down chitin particles, whereas initial densities of $2*10^4$ and $1*10^4$ cells/particle are not. B) Attachment rates of *psych6C06* to chitin hydrogel particles, measured for the initial cell densities shown in panel A. Lines are fit independently for each experiment and give the accumulation rate on the particle. The average attachment rate is $3.1*10^{-2} \pm 2.5*10^{-3}$ hr^{-1}. C) Detachment rates measured using chitin particles colonized for 10 h, and 24 h by an initial population of $4*10^4$ cells/particle. The slope of each line gives the rate at which cells leave the chitin particle at each timepoint. The average slope is $2.75*10^5 \pm 7*10^3$ cells/particle/hour. For A and B error bars are the SEM from a minimum of 11 measurements. D) Activity of *psych6C06* chitinases in culture supernatant (open symbols), and cell-associated (closed symbols) fractions. E) Activity of cell-associated chitinase for three different chitinase substrates (1, exochitinase-specific; 2, chitobiosidase-specific; 3, endochitinase specific). F) Yield of *psych6C06* cells grown on GlcNAc as the sole carbon source. Data points represent individual measurements. Line is a linear regression of the data, where the slope (0.89 ± 0.08 cells/GlcNAc w/w) gives the fractional yield. G) Measurements of *psych6C06* growth rate at nine different GlcNAc concentrations were fit to the Monod growth equation $\mu = \mu_{max}*S/(K_s + S)$, where μ is the observed exponential growth rate and S is the concentration of GlcNAc, to find the maximum growth rate (μ_{max}) and half-saturation constant (K_s). Bold lines indicate fits for each biological replicate (3x), dashed lines indicate 95% confidence intervals. The average μ_{max} is 0.37 ± 0.02 hr^{-1} (1.87 h doubling time) and K_s=1.1 ± 0.1 mg/L GlcNAc.

Table S1. Physiological parameters for microbial growth, metabolism and nutrient concentrations in the individual-based model.

Parameters	*Values (Units)*
μ_{max}: *maximum growth rate* (hr^{-1})	0.2-0.5*
K_s: *half saturation (mg/L)*	0.01-0.1*
Y: *growth yield* (*gr dry mass/gr substrate*)	0.5*
cell maintenance	0.1[f]
cell size (*μm*)	1 [f]
ρ: cell density (*mg* L^{-1})	2.9×10^{5} [f]
V_{1D} *: cell velocity at bulk solution (μm/s)*	10*
V_u *: median cell volume (fl)*	0.4 [f]
: enzyme production (gr enzyme/ gr biomass hr^{-1}*)*	0.05*
Tumbling frequency (s^{-1})	0.1[|]
X_0*: chemotactic sensitivity*(mm^2/hr)	446 [T]

[f] (2)
[|] (22)
[T] (8)
**Model assumption*

Table S2. The distribution range of the catalytic activity of various enzymes kcat. as a measure for particle lability from natural polymeric carbohydrates (Chitin, Alginate, Starch). The data are for various bacterial species with their corresponding abiotic conditions (species name, substrates and environmental conditions). Particle lability ($K_p = \alpha k_{cat} \left(\frac{Mw_{Oligomer}}{Mw_{Enyme}} \right) \times 3600$) is a compound parameter that is calculated from the product of the catalytic activity of the enzyme, k_{cat}, and the accessibility of cleavage sites within the polymer, α, which determines its lability. In the absence of measurements α is assumed to be one. k_{cat} is defined as the maximum number of polysaccharide molecules cleaved per second per enzyme. Mw represents the molecular weight for oligomers and enzymes.

Starch (alpha-amylase):

Turnover Number [1/S], k_{cat}.	***Particle*** lability, $K_{p,}$ ***[hr^{-1}]***	***Substrate***	***Species***	***Commentary***	***Literature***
140	3040.8	Pullulan	*Anabaena sp.*	wild-type enzyme	(23)
268	5820.96	maltotriose	*Anabaena sp.*	pH 4.5, 90°C, recombinant enzyme	(24)
283.3	6153.276	beta-cyclodextrin	*Anabaena sp.*	-	(25)
8.73	189.6156	4,6-ethylidene-[G7]-p-nitrophenyl-[G1]-alpha-D-maltoheptaoside	*Bacillus licheniformis*	wild-type, kcat/Km: 770000 1/s/M, 25°C, pH 6.0	(26)
34	738.48	4,6-ethylidene-[G7]-p-nitrophenyl-[G1]-alpha-D-maltoheptaoside	*Bacillus licheniformis*	wild-type, kcat/Km: 140000 1/s/M, 37°C, pH 4.5	(26)
205	4452.6	4,6-ethylidene-[G7]-p-nitrophenyl-[G1]-alpha-D-maltoheptaoside	*Bacillus licheniformis*	wild-type, kcat/Km: 1420000 1/s/M, 37°C, pH 6.5	(26)
0.156	3.38832	starch	*Bacillus megaterium*	15°C, pH 8.3	(27)
9.8	212.856	starch	*Bacillus megaterium*	mutant enzyme A53S, in the presence of 5 mM Ca^{2+}, in 20 mM Tris-HCl buffer (pH 7.2), at 30°C	(28)
19.9	432.228	starch	*Bacillus megaterium*	wild type enzyme, in the presence of 5 mM Ca^{2+}, in 20 mM Tris-HCl buffer (pH 7.2), at 30°C	(28)
0.025	0.543	soluble starch	*Bacillus sp.*	-	(25)
91.4	1985.208	starch	*Bacillus sp.*	pH 5.6, 40°C	(29)
98.3	2135.076	soluble starch	*Bacillus sp.*	-	(30)
31.1	675.492	beta-cyclodextrin	*Fusicoccum sp.*	pH 5.6, 40°C	(29)
196	4257.12	beta-cyclodextrin	*Fusicoccum sp.*	pH 4.5, 90°C, recombinant enzyme	(24)

3420	74282.4	soluble potato starch	*Fusicoccum sp.*	at 30°C in 10 mM MOPS buffer (pH 7.0) with 5 mM $CaCl_2$	(31)
0.02	0.4344	soluble starch	*Geobacillus thermoleovorans*	in 50 mM sodium phosphate buffer (pH 6.5) at 75°C	(32)
120	2606.4	starch	*Pseudoalteromonas haloplanktis*	wild-type enzyme	(23)
392	8514.24	4,6-ethylidene-[G7]-p-nitrophenyl-[G1]-alpha-D-maltoheptaoside	*Pseudoalteromonas haloplanktis*	15°C, pH 7.2	(33)
675	14661	4,6-ethylidene-[G7]-p-nitrophenyl-[G1]-alpha-D-maltoheptaoside	*Pseudoalteromonas haloplanktis*	pH not specified in the publication, 25°C	(34)
697	15138.84	4,6-ethylidene-[G7]-p-nitrophenyl-[G1]-alpha-D-maltoheptaoside	*Pseudoalteromonas haloplanktis*	25°C, pH 7.2	(33)
25.7	558.204	starch	*Pyrococcus furiosus*	wild type enzyme, in the absence of Ca^{2+}, in 20 mM Tris-HCl buffer (pH 7.2), at 30°C	(28)
29.4	638.568	beta-cyclodextrin	*Pyrococcus furiosus*	calculated as low molecular weight products	(35)
228	4952.16	acarbose	*Pyrococcus furiosus*	pH 4.5, 90°C, recombinant enzyme	(24)
241	5234.52	acarbose	*Pyrococcus furiosus*	pH 4.5, 90°C, recombinant enzyme	(24)
1940	42136.8	Dextrin	*Pyrococcus furiosus*	at 30°C in 10 mM MOPS buffer (pH 7.0) with 5 mM $CaCl_2$	(31)
130	2823.6	glycogen	*Pyrococcus sp.*	from rat liver, calculated as low molecular weight products	(35)
230	4995.6	acarbose	*Pyrococcus sp.*	short chain amylose, calculated as low molecular weight products	(35)
2280	49521.6	acarbose	*Pyrococcus sp.*	pH 6.5, 90°C	(36)
3000	65160	starch	*Pyrococcus sp.*	calculated as low molecular weight products	(37)
4180	90789.6	acarbose	*Pyrococcus sp.*	pH 6.5, 90°C	(36)
4680	101649.6	starch	*Pyrococcus sp.*	pH 6.5, 90°C	(36)
1457	31646.04	starch	*Streptomyces megasporus*	pH not specified in the publication, 55°C	(34)
0.085	1.8462	Pullulan	*Thermoactinomyces vulgaris*	pH 5.6, 40°C	(29)
67	1455.24	starch	*Thermoactinomyces vulgaris*	pH 4.5, 90°C, recombinant enzyme	(24)
153	3323.16	4,6-ethylidene-[G7]-p-nitrophenyl-[G1]-alpha-D-maltoheptaoside	*Thermobifida fusca*	pH not specified in the publication, 25°C	(34)

1.6	34.752	maltotriose	*Thermotoga neapolitana*	-	(35)
34	738.48	4-nitrophenyl alpha-D-maltohexaoside	*Thermotoga neapolitana*	in 50 mM sodium phosphate buffer (pH 6.5) at 75°C	(32)
37.2	807.984	maltopentaose	*Thermotoga neapolitana*	pH 5.6, 40°C	(29)
1920	41702.4	rabbit glycogen	*Thermotoga neapolitana*	at 30°C in 10 mM MOPS buffer (pH 7.0) with 5 mM $CaCl_2$	(31)

Alginate lyase:

guluronate-specific alginate lyase

Turnover Number [1/s] , k_{cat}.	***Particle* lability, K_p, [hr^{-1}]**	***Substrate***	***Species***	***Commentary***	***Literature***
936	24261.12	alginate	*Flavobacterium sp.*	pH 8.5, 30°C	(38)
872.8	22622.98	sodium alginate	*Flavobacterium sp.*	recombinant His-tagged enzyme, pH 8.5, 45°C	(38)
32	829.44	alginate	*Pseudomonas aeruginosa*	pH 7.1, 25°C	(39)
32	829.44	poly-(beta-(1->4)-D-mannuronan)	*Pseudomonas aeruginosa*	pH 7.1, 25°C	(39)
1.5	38.88	acetylated poly-(beta-(1->4)-D-mannuronan)	*Pseudomonas aeruginosa*	pH 7.1, 25°C	(39)
1.2	31.104	acetylated alginate	*Pseudomonas aeruginosa*	pH 7.1, 25°C	(39)
56.9	1474.848	sodium alginate	*Saccharophagus degradans*	pH 7.5, 30°C, wild-type enzyme	(40)
19.51	505.6992	sodium alginate	*Zobellia galactanivorans*	with L-guluronate content of 33.3%, pH 7.5, 30°C, recombinant enzyme	(41)
17.89	463.7088	sodium alginate	*Zobellia galactanivorans*	with L-guluronate content of 52.6%, pH 7.5, 30°C, recombinant enzyme	(41)
12.66	328.1472	sodium alginate	*Zobellia galactanivorans*	with L-guluronate content of 66.7%, pH 7.5, 30°C, recombinant enzyme	(41)

mannuronate-specific alginate lyase

Turnover Number [1/S] , k_{cat}.	***Particle* lability, K_p, [hr^{-1}]**	***Substrate***	***Species***	***Commentary***	***Literature***
2.42	62.7264	alginate	*Pseudomonas aeruginosa*	protein PA1167, pH 7.5, 37°C	(42)
748	19388.16	alginate	*Pseudomonas aeruginosa*	AlgL	(42)

7.6	196.992	hepta-alpha1,4-L-guluronate	*Alteromonas sp.*	pH 8.5, 30°C	(42)
13.2	342.144	hepta-beta1,4-D-mannuronate	*Alteromonas sp.*	pH 8.5, 30°C	(42)
7.9	204.768	hexa-alpha1,4-L-guluronate	*Alteromonas sp.*	pH 8.5, 30°C	(42)
11.9	308.448	hexa-beta1,4-D-mannuronate	*Alteromonas sp.*	pH 8.5, 30°C	(42)
7.8	202.176	nona-alpha1,4-L-guluronate	*Alteromonas sp.*	pH 8.5, 30°C	(42)
10.8	279.936	nona-beta1,4-D-mannuronate	*Alteromonas sp.*	pH 8.5, 30°C	(42)
7.3	189.216	octa-alpha1,4-L-guluronate	*Alteromonas sp.*	pH 8.5, 30°C	(42)
11.1	287.712	octa-beta1,4-D-mannuronate	*Alteromonas sp.*	pH 8.5, 30°C	(42)
6.2	160.704	penta-alpha1,4-L-guluronate	*Alteromonas sp.*	pH 8.5, 30°C	(42)
7.4	191.808	penta-beta1,4-D-mannuronate	*Alteromonas sp.*	pH 8.5, 30°C	(42)
0.057	1.47744	sodium alginate	*Saccharophagus degradans*	pH 7.5, 30°C, H415A	(40)
56.9	1474.848	sodium alginate	*Saccharophagus degradans*	pH 7.5, 30°C, wild-type enzyme	(40)
2.5	64.8	tetra-alpha1,4-L-guluronate	*Alteromonas sp.*	pH 8.5, 30°C	(43)
3.2	82.944	tetra-beta1,4-D-mannuronate	*Alteromonas sp.*	pH 8.5, 30°C	(43)

Chitin (Chitinase)

Turnover Number [1/S] , k_{cat}.	***Particle*** lability, ***K_p, [hr^{-1}]***	***Substrate***	***Species***	***Commentary***	***Literature***
110.6	2933.112	4-methylumbelliferyl-N,N',N''-triacetylchitotriose	*Vibrio parahaemolyticus*	pH 7, 37°C, VpChiA	(44)
13.94	369.6888	4-methylumbelliferyl-N,N'-diacetylchitobiose	*Vibrio parahaemolyticus*	pH 7, 37°C, VpChiA	(44)
0.383	10.15716	p-nitrophenol-beta-D-N,N'-diacetylchitobioside	*Vibrio harveyi*	70°C, pH 7	(45)
2.9	76.908	chitohexaose	*Vibrio harveyi*	pH 5.5, 37°C, wild-type enzyme	(46)
2.37	62.8524	colloidal chitin	*Vibrio harveyi*	pH 7.0, 40°C	(47)
1.2	31.824	chitin	*Vibrio harveyi*	pH 5.5, 37°C, colloidal chitin, wild-type enzyme	(46)
0.21	5.5692	GlcNAcbeta(1-	*Vibrio harveyi*	wild-type, 37°C	(48)

		4)GlcNAcbeta(1-4)GlcNAcbeta(1-4)GlcNAcbeta(1-4)GlcNAc			
0.19	5.0388	GlcNAcbeta(1-4)GlcNAcbeta(1-4)GlcNAcbeta(1-4)GlcNAcbeta(1-4)GlcNAc	*Vibrio harveyi*	wild-type, 37°C	(48)
0.032	0.84864	p-nitrophenol-beta-D-mannopyranoside	*Vibrio harveyi*	-	(45)
0.005	0.1326	chitin	*Thermococcus chitonophagus*	-	(45)
67.4	1787.448	4-methylumbelliferyl-beta-D-N,N',N''-triacetylchitotrioside	*Serratia marcescens*	pH 6.5, isozyme ChiA	(49)
56.8	1506.336	4-methylumbelliferyl-beta-D-N,N',N''-triacetylchitotrioside	*Serratia marcescens*	pH 6.5, isozyme ChiB	(49)
2	53.04	4-methylumbelliferyl-beta-D-N,N',N''-triacetylchitotrioside	*Serratia marcescens*	pH 6.5, isozyme ChiC	(49)
2.2	58.344	beta-chitin	*Serratia marcescens*	pH 6.1, 37°C	(50)
1.7	45.084	beta-chitin	*Serratia marcescens*	pH 8.0, 37°C; pH 8.0, 37°C	(50)
6.7	177.684	4-nitrophenyl chitobioside	*Pyrococcus furiosus*	pH 4.8, 50°C, wild-type enzyme	(51)
0.1	2.652	colloidal chitin	*Penicillium ochrochloron*	wild-type, 37°C	(48)
9.6	254.592	4-nitrophenyl N,N'-diacetyl-beta-D-chitobioside	*Paenibacillus thermoaerophilus*	pH 7.0, 60°C	(52)
0.99	26.2548	4-nitrophenyl N,N'-diacetylchitobiose	*Paenibacillus sp.*	recombinant enzyme, pH 5.5, 37°C	(53)
83.46	2213.359	chitin	*Paenibacillus sp.*	pH 5.0, 50°C	(54)
19.54	518.2008	4-nitrophenyl-beta-1,4-N,N'-diacetyl-chitobiose	*Moritella marina*	pH 5.0, 28°C, purified recombinant enzyme	(55)
11.88	315.0576	4-nitrophenyl-beta-1,4-N,N'-diacetyl-chitobiose	*Moritella marina*	pH 5.0, 20°C, purified recombinant enzyme	(55)
7.33	194.3916	4-nitrophenyl-beta-1,4-N,N'-diacetyl-chitobiose	*Moritella marina*	pH 5.0, 15°C, purified recombinant enzyme	(55)
5.46	144.7992	4-nitrophenyl-beta-1,4-N,N'-diacetyl-chitobiose	*Moritella marina*	pH 5.0, 10°C, purified recombinant enzyme	(55)

4.33	114.8316	4-nitrophenyl-beta-1,4-N,N'-diacetyl-chitobiose	*Moritella marina*	pH 5.0, 5°C, purified recombinant enzyme	(55)
0.79	20.9508	4-nitrophenyl-beta-1,4-N,N'-diacetyl-chitobiose	*Moritella marina*	pH 5.0, 0°C, purified recombinant enzyme	(55)
0.5	13.26	chitohexaose	*Coccidioides immitis*	30°C	(56)
18	477.36	4-methylumbelliferyl-N,N'-diacetylchitobiose	*Chromobacterium sp.*	pH 7.0, 37°C, wild-type enzyme	(57)
0.43	11.4036	4-nitrophenyl-chitobiose	*Bacillus licheniformis*	wild-type, strain DSM13, pH 6.0, 37°C	(58)
0.31	8.2212	4-nitrophenyl-chitobiose	*Bacillus licheniformis*	pH 6.0, 37°C	(59)
0.31	8.2212	4-nitrophenyl-chitobiose	*Bacillus licheniformis*	wild-type, strain DSM8785, pH 6.0, 37°C	(58)
0.17	4.5084	4-nitrophenyl-chitobiose	*Bacillus licheniformis*	wild-type, strain DSM13, pH 3.0, 37°C	(58)
0.14	3.7128	4-nitrophenyl-chitobiose	*Bacillus licheniformis*	wild-type, strain DSM8785, pH 3.0, 37°C	(58)
22.4	594.048	4-methylumbelliferyl-tri-N-acetylchitotriose	*Bacillus circulans*	37°C, pH 6, wild-type	(60)
26.9	713.388	reduced chitopentaose	*Bacillus circulans*	37°C, pH 6, wild-type	(60)
2.15	57.018	p-nitrophenyl-N,N'-diacetylchitobiose	*Bacillus circulans*	pH 5.0, 30°C, wild-type enzyme	(61)
9.55	253.266	carboxymethyl chitin	*Bacillus circulans*	37°C, pH 6, wild-type	(60)
0.0007	0.018564	4-methylumbelliferyl GlcNAcbeta(1-4)GlcNAcbeta(1-4)GlcNAc	*Aeromonas caviae*	pH 6.0, 50°C, recombinant His-tagged wild-type enzyme	(62)
0.006	0.15912	4-methylumbelliferyl-GlcNAcbeta(1->4)GlcNAc	*Aeromonas caviae*	pH 6.0, 50°C, recombinant His-tagged wild-type enzyme	(62)

Table S3. Particle associated cell density at different water solutions and seasons in the Baltic Sea. The data are extracted from Rieck et al., 2015 (63). The data on particle size range and number of particles per one litter of solution are used from field studies (64) to estimate the number of cells per single particles across observed size ranges. The simulations are performed for three initial cell densities for approximately the mean particle lability observed for natural biopolymers (K_p~100hr^{-1}, Figure 1B) and POM uptake efficiency is estimated after 10hours. The simulation data are used to predict uptake efficiency from natural marine snow.

	Summer			**Winter/fall**			**Simulations (this study)**		
	Marine	Mesohaline	Oligohaline	Marine	Mesohaline	Oligohaline			
Particle-associated cell density [cells L^{-1}](63)	0.26 (±0.06)×10^8	0.57 (± 0.13) ×10^8	0.76 (± 0.21) ×10^8	0.12 (± 0.069) ×10^8	0.13 (± 0.08) ×10^8	0.74 (± 0.03)×10^8	1000*	5000*	10000*
Particle size range (mm)(63)	0.2-7(mean 0.5)	0.2-7(mean 0.5)	0.2-7(mean 0.5)	0.2-7(mean 0.5)	0.2-7(mean 0.5)	0.2-7(mean 0.5)	0.2	0.2	0.2
Number of particles per L(64)	≤28 (mean 6.4)	≤28 (mean 6.4)	≤28 (mean 6.4)	≤28 (mean 6.4)	≤28 (mean 6.4)	≤28 (mean 6.4)	----	-----	-----
Total cell fraction per particle	0.2mm:1.8%; 7mm:98.2%	0.2mm:1.8%; 7mm:98.2%	0.2mm:1.8%; 7mm:98.2%	0.2mm:1.8%; 7mm:98.2%	0.2mm:1.8%; 7mm:98.2%	0.2mm:1.8%; 7mm:98.2%	----	-----	-----
Cells per particle									
0.2 mm	7.80E+04	1.71E+05	2.28E+05	3.60E+04	3.90E+04	2.32E+05	8.83E+03^T	2.10E+05^T	6.32E+05^T
7 mm	8.51E+07	1.87E+08	2.49E+08	3.93E+07	4.26E+07	2.42E+08	----	-----	-----
Estimated POM Uptake efficiency									
0.2 mm	0.041	0.057	0.061	0.03	0.032	0.07	0.025	0.064	0.08

^{T} cell numbers after 10hours

*initial cell number for simulation

References for SI Appendix

1. Ebrahimi AN, Or D (2014) Microbial dispersal in unsaturated porous media: Characteristics of motile bacterial cell motions in unsaturated angular pore networks. *Water Resour Res* 50(9):7406–7429.
2. Kreft JU, Booth G, Wimpenny JWT (1998) BacSim, a simulator for individual-based modelling of bacterial colony growth. *Microbiology* 144(12):3275–3287.
3. Monod J (1949) The Growth of Bacterial Cultures. *Annu Rev Microbiol* 3(1):371–394.
4. Mitchell JG, Kogure K (2006) Bacterial motility: links to the environment and a driving force for microbial physics. *FEMS Microbiol Ecol* 55(1):3–16.
5. Son K, Brumley DR, Stocker R (2015) Live from under the lens: Exploring microbial motility with dynamic imaging and microfluidics. *Nat Rev Microbiol* 13(12):761–775.
6. Kim M, Or D (2016) Individual-based model of microbial life on hydrated rough soil surfaces. *PLoS One* 11(1):e0147394.
7. Hillen T, Painter KJ (2009) A user's guide to PDE models for chemotaxis. *J Math Biol* 58(1–2):183–217.
8. Ahmed T, Stocker R (2008) Experimental verification of the behavioral foundation of bacterial transport parameters using microfluidics. *Biophys J* 95(9):4481–4493.
9. Berne C, Ducret A, Hardy GG, Brun Y V. (2015) Adhesins involved in attachment to abiotic surfaces by Gram-negative bacteria. *Microbiol Spectr*. doi:10.1128/microbiolspec.mb-0018-2015.
10. Ebrahimi A, Or D (2018) On upscaling of soil microbial processes and biogeochemical fluxes from aggregates to landscapes. *J Geophys Res Biogeosciences*. doi:10.1029/2017JG004347.
11. Grunwald P (1989) Determination of effective diffusion coefficients - an important parameters for the efficiency of immobilized biocatalysts. *Biochem Educ*. doi:10.1016/0307-4412(89)90018-6.
12. Schimel JP, Weintraub MN (2003) The implications of exoenzyme activity on microbial carbon and nitrogen limitation in soil: A theoretical model. *Soil Biol Biochem* 35(4):549–563.
13. Drake JE, et al. (2013) Stoichiometry constrains microbial response to root exudation-insights from a model and a field experiment in a temperate forest. *Biogeosciences* 10(2):821–838.
14. Ebrahimi A, Or D (2017) Mechanistic modeling of microbial interactions at pore to profile scale resolve methane emission dynamics from permafrost soil. *J Geophys Res*

Biogeosciences 122(5):1216–1238.

15. Gore J, Youk H, van Oudenaarden A (2009) Snowdrift game dynamics and facultative cheating in yeast. *Nature* 459(7244):253–256.
16. Enke TN, Leventhal GE, Metzger M, Saavedra JT, Cordero OX (2018) Microscale ecology regulates particulate organic matter turnover in model marine microbial communities. *Nat Commun* 9(1):2743.
17. Datta MS, Sliwerska E, Gore J, Polz M, Cordero OX (2016) Microbial interactions lead to rapid micro-scale successions on model marine particles. *Nat Commun* 7(May):11965.
18. Scott M, Gunderson CW, Mateescu EM, Zhang Z, Hwa T (2010) Interdependence of cell growth and gene expression: Origins and consequences. *Science (80-)* 330(6007):1099–1102.
19. Miller GL (1959) Use of dinitrosalicylic acid reagent for determination of reducing sugar. *Anal Chem* 31(3):426–428.
20. Dennis PP, Bremer H (2008) Modulation of chemical composition and other parameters of the cell at different exponential growth rates. *EcoSal Plus* 3(1). doi:10.1128/ecosal.5.2.3.
21. Baldwin WW, Myer R, Kung T, Anderson E, Koch AL (1995) Growth and Buoyant Density of Escherichia coli at Very Low Osmolarities. *J Bacteriol 177(1), 235-237.*
22. Kiørboe T, Grossart HP, Ploug H, Tang K (2002) Mechanisms and rates of bacterial colonization of sinking aggregates. *Appl Environ Microbiol* 68(8):3996–4006.
23. Mizuno M, et al. (2004) The crystal structure of *Thermoactinomyces vulgaris* R-47 α-amylase II (TVA II) complexed with transglycosylated product. *Eur J Biochem*. doi:10.1111/j.1432-1033.2004.04183.x.
24. Yang SJ, et al. (2004) Enzymatic analysis of an amylolytic enzyme from the hyperthermophilic archaeon *Pyrococcus furiosus* reveals its novel catalytic properties as both an α-amylase and a cyclodextrin-hydrolyzing enzyme. *Appl Environ Microbiol*. doi:10.1128/AEM.70.10.5988-5995.2004.
25. Champreda V, Kanokratana P, Sriprang R, Tanapongpipat S, Eurwilaichitr L (2007) Purification, biochemical characterization, and gene cloning of a new extracellular thermotolerant and glucose tolerant maltooligosaccharide-forming α-amylase from an endophytic ascomycete *Fusicoccum sp.* BCC4124 . *Biosci Biotechnol Biochem*. doi:10.1271/bbb.70198.
26. Liu YH, Lu FP, Li Y, Wang JL, Gao C (2008) Acid stabilization of *Bacillus licheniformis* alpha amylase through introduction of mutations. *Appl Microbiol Biotechnol*. doi:10.1007/s00253-008-1580-5.

27. Vester JK, Glaring MA, Stougaard P (2015) An exceptionally cold-adapted alpha-amylase from a metagenomic library of a cold and alkaline environment. *Appl Microbiol Biotechnol*. doi:10.1007/s00253-014-5931-0.
28. Ghollasi M, Khajeh K, Naderi-Manesh H, Ghasemi A (2010) Engineering of a bacillus α-amylase with improved thermostability and calcium independency. *Appl Biochem Biotechnol*. doi:10.1007/s12010-009-8879-2.
29. Kato S, et al. (2007) Molecular cloning and characterization of an α-amylase from *Pichia burtonii* 15-1 . *Biosci Biotechnol Biochem*. doi:10.1271/bbb.70407.
30. Uma Maheswar Rao JL, Satyanarayana T (2007) Purification and characterization of a hyperthermostable and high maltogenic α-amylase of an extreme thermophile *Geobacillus thermoleovorans*. *Appl Biochem Biotechnol*. doi:10.1007/s12010-007-0017-4.
31. Reyes-Sosa FM, Molina-Heredia FP, De La Rosa MA (2010) A novel α-amylase from the cyanobacterium *Nostoc sp.* PCC 7119. *Appl Microbiol Biotechnol*. doi:10.1007/s00253-009-2191-5.
32. Park KM, et al. (2010) Characterization of an exo-acting intracellular α-amylase from the hyperthermophilic bacterium *Thermotoga neapolitana*. *Appl Microbiol Biotechnol*. doi:10.1007/s00253-009-2284-1.
33. D'Amico S, Gerday C, Feller G (2003) Temperature adaptation of proteins: Engineering mesophilic-like activity and stability in a cold-adapted α-amylase. *J Mol Biol*. doi:10.1016/j.jmb.2003.07.014.
34. Cipolla A, Delbrassine F, Da Lage JL, Feller G (2012) Temperature adaptations in psychrophilic, mesophilic and thermophilic chloride-dependent alpha-amylases. *Biochimie*. doi:10.1016/j.biochi.2012.05.013.
35. De Mot R, Verachtert H (1987) Purification and characterization of extracellular α-amylase and glucoamylase from the yeast *Candida antarctica* CBS 6678. *Eur J Biochem*. doi:10.1111/j.1432-1033.1987.tb11175.x.
36. Tachibana Y, Fujiwara S, Takagi M, Imanaka T (1997) Cloning and expression of the 4-α-glucanotransferase gene from the hyperthermophilic archaeon *Pyrococcus sp.* KOD1, and characterization of the enzyme. *J Ferment Bioeng*. doi:10.1016/S0922-338X(97)81134-8.
37. Dey S, Agarwal SO (1999) Characterization of a thermostable α-amylase from a thermophilic *Streptomyces megasporus* strain SD12. *Indian J Biochem Biophys*.
38. Huang L, et al. (2013) Characterization of a new alginate lyase from newly isolated *Flavobacterium sp.* S20. *J Ind Microbiol Biotechnol*. doi:10.1007/s10295-012-1210-1.

39. Farrell EK, Tipton PA (2012) Functional characterization of AlgL, an alginate lyase from *Pseudomonas aeruginosa*. *Biochemistry*. doi:10.1021/bi301425r.
40. Park D, Jagtap S, Nair SK (2014) Structure of a PL17 family alginate lyase demonstrates functional similarities among exotype depolymerases. *J Biol Chem*. doi:10.1074/jbc.M113.531111.
41. Thomas F, et al. (2013) Comparative characterization of two marine alginate lyases from *Zobellia galactanivorans* reveals distinct modes of action and exquisite adaptation to their natural substrate. *J Biol Chem*. doi:10.1074/jbc.M113.467217.
42. Yamasaki M, et al. (2004) Structure and function of a hypothetical *Pseudomonas aeruginosa* protein PA1167 classified into family PL-7: A novel alginate lyase with a β-sandwich fold. *J Biol Chem*. doi:10.1074/jbc.M402466200.
43. Iwamoto Y, et al. (2001) Purification and characterization of bifunctional alginate lyase from *Alteromonas sp.* Strain No. 272 and its action on saturated oligomeric substrates. *Biosci Biotechnol Biochem* 65(1):133–142.
44. Chuang HH, Lin FP (2007) New role of C-terminal 30 amino acids on the insoluble chitin hydrolysis in actively engineered chitinase from *Vibrio parahaemolyticus*. *Appl Microbiol Biotechnol* 76(1):123–133.
45. Andronopoulou E, Vorgias CE (2003) Purification and characterization of a new hyperthermostable, allosamidin-insensitive and denaturation-resistant chitinase from the hyperthermophilic archaeon *Thermococcus chitonophagus*. *Extremophiles*. doi:10.1007/s00792-002-0294-3.
46. Pantoom S, Songsiriritthigul C, Suginta W (2008) The effects of the surface-exposed residues on the binding and hydrolytic activities of *Vibrio carchariae* chitinase A. *BMC Biochem*. doi:10.1186/1471-2091-9-2.
47. Patil NS, Waghmare SR, Jadhav JP (2013) Purification and characterization of an extracellular antifungal chitinase from *Penicillium ochrochloron* MTCC 517 and its application in protoplast formation. *Process Biochem*. doi:10.1016/j.procbio.2012.11.017.
48. Suginta W, Pantoom S, Prinz H (2009) Substrate binding modes and anomer selectivity of chitinase A from *Vibrio harveyi*. *J Chem Biol*. doi:10.1007/s12154-009-0021-y.
49. Synstad B, et al. (2008) Expression and characterization of endochitinase C from *Serratia marcescens* BJL200 and its purification by a one-step general chitinase purification method . *Biosci Biotechnol Biochem*. doi:10.1271/bbb.70594.
50. Hamre AG, Eide KB, Wold HH, Sørlie M (2015) Activation of enzymatic chitin degradation by a lytic polysaccharide monooxygenase. *Carbohydr Res*. doi:10.1016/j.carres.2015.02.010.

51. Tsuji H, et al. (2010) Kinetic and crystallographic analyses of the catalytic domain of chitinase from *Pyrococcus furiosus*- the role of conserved residues in the active site. *FEBS J*. doi:10.1111/j.1742-4658.2010.07685.x.
52. Ueda J, Kurosawa N (2015) Characterization of an extracellular thermophilic chitinase from *Paenibacillus thermoaerophilus* strain TC22-2b isolated from compost. *World J Microbiol Biotechnol*. doi:10.1007/s11274-014-1754-5.
53. Itoh T, et al. (2014) Overexpression, purification, and characterization of *Paenibacillus* cell surface-expressed chitinase ChiW with two catalytic domains. *Biosci Biotechnol Biochem*. doi:10.1080/09168451.2014.891935.
54. Singh AK, Chhatpar HS (2011) Purification and characterization of chitinase from *Paenibacillus sp.* D1. *Appl Biochem Biotechnol*. doi:10.1007/s12010-010-9116-8.
55. Stefanidi E, Vorgias CE (2008) Molecular analysis of the gene encoding a new chitinase from the marine psychrophilic bacterium *Moritella marina* and biochemical characterization of the recombinant enzyme. *Extremophiles*. doi:10.1007/s00792-008-0155-9.
56. Fukamizo T, Sasaki C, Schelp E, Bortone K, Robertus JD (2001) Kinetic properties of chitinase-1 from the fungal pathogen *Coccidioides immitis*. *Biochemistry*. doi:10.1021/bi001537s.
57. Park SK, Kim CW, Kim H, Jung JS, Harman GE (2007) Cloning and high-level production of a chitinase from *Chromobacterium sp*. and the role of conserved or nonconserved residues on its catalytic activity. *Appl Microbiol Biotechnol*. doi:10.1007/s00253-006-0614-0.
58. Songsiriritthigul C, Pesatcha P, Eijsink VGH, Yamabhai M (2009) Directed evolution of a Bacillus chitinase. *Biotechnol J*. doi:10.1002/biot.200800258.
59. Songsiriritthigul C, Lapboonrueng S, Pechsrichuang P, Pesatcha P, Yamabhai M (2010) Expression and characterization of *Bacillus licheniformis* chitinase (ChiA), suitable for bioconversion of chitin waste. *Bioresour Technol*. doi:10.1016/j.biortech.2010.01.036.
60. Watanabe T, et al. (2003) Aromatic residues within the substrate-binding cleft of *Bacillus circulans* chitinase A1 are essential for hydrolysis of crystalline chitin. *Biochem J*. doi:10.1042/bj20030419.
61. Suginta W, Songsiriritthigul C, Kobdaj A, Opassiri R, Svasti J (2007) Mutations of Trp275 and Trp397 altered the binding selectivity of *Vibrio carchariae* chitinase A. *Biochim Biophys Acta - Gen Subj*. doi:10.1016/j.bbagen.2007.03.012.
62. Lin FP, et al. (2009) Effects of C-terminal amino acids truncation on enzyme properties of *Aeromonas caviae* D1 chitinase. *Arch Microbiol*. doi:10.1007/s00203-008-0451-x.

63. Rieck A, Herlemann DPR, Jürgens K, Grossart HP (2015) Particle-associated differ from free-living bacteria in surface waters of the baltic sea. *Front Microbiol* 6(DEC). doi:10.3389/fmicb.2015.01297.
64. Möller KO, et al. (2012) Marine snow, zooplankton and thin layers: Indications of a trophic link from small-scale sampling with the Video Plankton Recorder. *Mar Ecol Prog Ser* 468:57–69.